AGU PUBLICATIONS

JGR

Journal of Geophysical Research: Solid Earth

RESEARCH ARTICLE

10.1002/2014JB011162

Key Points:
- Rayleigh wave D/P ratio method
- Shear wave speed and thickness of marine sediment
- Shear wave traveltime delays caused by sediments

Correspondence to:
Y. Ruan,
youyi_ruan@brown.edu

Citation:
Ruan, Y., D. W. Forsyth, and S. W. Bell (2014), Marine sediment shear velocity structure from the ratio of displacement to pressure of Rayleigh waves at seafloor, *J. Geophys. Res. Solid Earth*, *119*, doi:10.1002/2014JB011162.

Received 28 MAR 2014
Accepted 13 JUL 2014
Accepted article online 17 JUL 2014

Marine sediment shear velocity structure from the ratio of displacement to pressure of Rayleigh waves at seafloor

Youyi Ruan[1], Donald W. Forsyth[1], and Samuel W. Bell[1]

[1]Department of Geological Sciences, Brown University, Providence, Rhode Island, USA

Abstract The complex ratio of vertical displacement to pressure (D/P) at seafloor is a function of frequency. It is sensitive to the subsurface elastic properties, particularly the shear modulus, and therefore can be used to determine the shear velocity and thickness of marine sediments. Instead of using compliance in response to loading of long-period infragravity waves as in previous studies, we investigate the transfer function from pressure to displacement using Rayleigh waves generated by microseisms and earthquakes. We find that at frequencies between 0.1 and 0.2 Hz, the Rayleigh wave transfer function is very sensitive to marine sediments and can be reliably obtained from microseism noise. Using a surface wave mode method, we calculate synthetic D/P ratios and examine their sensitivity to water depth, shear wave speed, and thickness of sediments. We develop a method to invert the Rayleigh wave D/P ratio for a regional 1-D profile of sediment shear wave speed and associated sediment thickness beneath each ocean bottom seismograph (OBS). We apply our method to a group of deep water OBSs deployed in the Cascadia Initiative and obtain a well-resolved depth-dependent shear wave speed for sediments on the Juan de Fuca plate and shear wave traveltime delays caused by sediments at each station.

1. Introduction

The reliable determination of the structure of marine sediments has important applications in many different fields. The growing interest in continental margins and the development of instruments and techniques have resulted in large-scale seismic experiments involving deployment of ocean bottom seismographs (OBS). Due to their very low shear wave speed [e.g., *Hamilton*, 1971], sediments beneath the OBS could have important effect on shear wave traveltime measurements and therefore need to be considered in seismic tomography of the oceanic crust and mantle. The elastic properties of soft marine sediments are also responsible for strong site effects, so any seismic studies using amplitude data may be biased if the site effect is ignored. Moreover, seismic or acoustic modeling and offshore drilling hazard assessment also will benefit from well-constrained sediment structures.

Active seismic methods have been commonly used to determine the depth of sediment layers and compressional wave speed profiles. The shear wave speed of sediments, however, has often not been well constrained. Direct measurement of sediment shear properties is difficult because active sources in water requires strong energy conversion to produce appreciable shear wave phases on seafloor; only a few such measurements have been reported [e.g., *Berge et al.*, 1990; *Ewing et al.*, 1992; *Tinivella and Accaino*, 2000]. Other than using body shear waves, *Nolet and Dorman* [1996] have investigated the shear wave speed and attenuation by modeling the waveforms of interface (Scholte) waves—a surface wave with energy mostly concentrated on the liquid-solid boundary. In a recent active source seismic survey, *Kugler et al.* [2007] used Scholte waves in surface wave tomography to image 3-D shear wave speed of shallow water marine sediments. Due to the limitation of source energy, all these studies can only resolve the sediment structures at very shallow depth (< 100 m).

Compliance methods have also been used to constrain marine sediments. Seafloor compliance can be described by the complex transfer function from pressure to vertical displacement, multiplied by the wave number, as a function of frequency. On the ocean bottom, the pressure field generated by ocean water waves (mostly infragravity waves in deep water) deforms the seafloor, resulting in vertical displacement. The deformation of the seafloor depends on the elastic properties of subsurface structures, primarily the shear modulus. Seafloor compliance therefore can be used to determine shear velocity of marine sediments

and underlying igneous crust. The compliance method was first used by *Yamamoto and Torii* [1986] and *Yamamoto et al.* [1989] for seabed structures and extended by *Crawford et al.* [1991] to image the structure of oceanic crust and uppermost mantle. Gravity wave compliance also has been used for subbasalt sediments [*Crawford*, 2004]. In deep water, the primary limitation on the upper frequency limit is the depth penetration of the water waves; at short periods, the pressure variations do not extend to the seafloor. In 3000 m of water, for example, the high-frequency cutoff is 0.02 to 0.03 Hz. In shallower water, the primary limitation is often the presence of overwhelming microseism noise at frequencies higher than 0.1 Hz. In very shallow water (< 100 m) infragravity waves may dominate the noise signals again [*Webb and Crawford*, 2010].

In this paper, we investigate the transfer functions from pressure to vertical displacement obtained for Rayleigh waves generated either by earthquakes or microseisms. Although using the same basic measurements as in the infragravity wave compliance method, albeit in a different frequency range, we do not use the term "compliance" because the displacement and pressure are both integral properties of the same propagating Rayleigh waves rather than the displacement being in response to external pressure forcing as with water waves. Instead, we simply use amplitude and phase to describe the complex transfer function or "D/P ratio" as an abbreviated way to refer to the amplitude of the transfer function. Admittance is another term for transfer function [*Munk and Cartwright*, 1966]; when the two fields being related are expected to be in phase, as for Rayleigh waves, then admittance is commonly used as shorthand for amplitude of the transfer function [e.g., *McKenzie and Bowin*, 1976; *Forsyth*, 1985]. We briefly outline the observation of seafloor transfer functions from both microseism noise and earthquake-generated Rayleigh waves, and then investigate the sensitivity of the D/P ratio to shear wave speed and thickness of sediments. Finally, we invert the frequency-dependent D/P ratio observed at deep water OBSs deployed in the Cascadia Initiative (Figure 1) for the sediment structures beneath them. In addition, we discuss the possible factors that may affect the uncertainty and validity of this method.

2. Rayleigh Wave D/P Ratios in the Microseism Band

Measurement of gravity wave compliance is usually made from the spectra of pressure and acceleration in the frequency range from 0.001 to 0.03 Hz [e.g., *Crawford et al.*, 1991; *Crawford*, 2004]. Although in *Crawford et al.* [1991], high coherence between seafloor pressure and vertical acceleration in the microseism band (0.1–0.2 Hz) has been observed, the compliance method has not been used in this band because the presence of strong microseism noise. Microseism noise is generated by the interaction of two opposing surface gravity waves whose effects penetrate down to the seafloor [e.g., *Longuet-Higgins*, 1950; *Cooper and Longuet-Higgins*, 1955; *Kedar et al.*, 2008; *Ardhuin et al.*, 2011; *Bromirski et al.*, 2013]. Away from the source, microseisms are mostly Rayleigh waves that can propagate great distances with little attenuation. *Bradner* [1963] suggested that the displacement to pressure transfer function in the microseism band could be used to determine subsurface structure, but to our knowledge no one has made practical use of that suggestion. In our D/P ratio method, we define seismic-wave admittance at the seafloor as the linear transfer function from differential pressure to vertical displacement at the seafloor as a function of frequency,

$$\eta(\omega) = \frac{u_z(\omega)}{\Delta P(\omega)}, \tag{1}$$

where u_z is vertical displacement, ΔP is the differential pressure, and ω is angular frequency. This definition is convenient because it is easy and straightforward for the other use of the transfer function, i.e., removing noise from the vertical component using pressure variations recorded by differential pressure gauge (DPG) records [*Crawford and Webb*, 2000]. In practice, to avoid bias in the presence of noise, we calculate the transfer function from

$$\eta(\omega) = \frac{\langle u_z(\omega) \cdot \Delta P^*(\omega) \rangle}{\langle \Delta P(\omega) \cdot \Delta P^*(\omega) \rangle}, \tag{2}$$

where the angle brackets indicate averaging over a number of individual time windows or samples, and the asterisk indicates the complex conjugate.

We investigated seismic noise in the first year of data from OBS deployed in the Cascadia Initiative. Due to strong bottom currents, horizontal components at long periods generally have orders of magnitude higher noise levels than the vertical component. When seismometers are slightly tilted, horizontal noise will leak

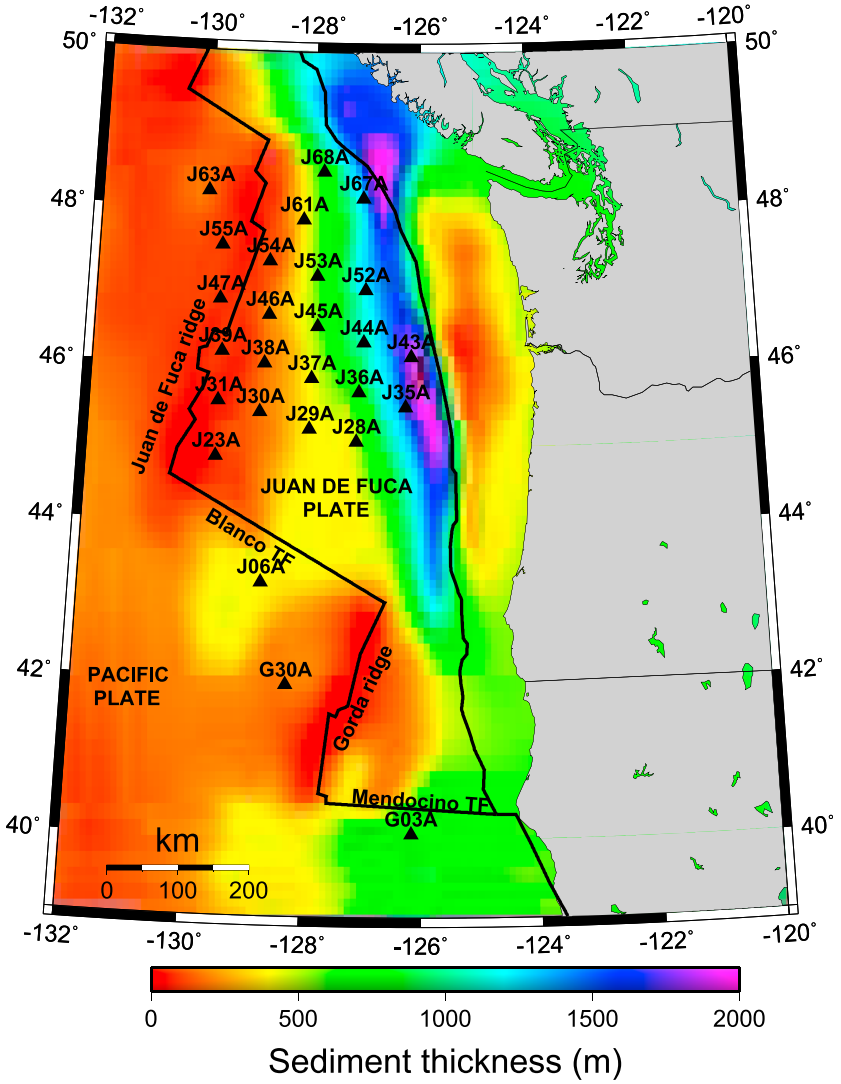

Figure 1. Deep water OBS stations deployed during the first year of Cascadia Initiative. Background map is the reference sediment thickness from a National Oceanic and Atmospheric Administration (NOAA) report [*Divins*, 2003] of global sediment thickness based on seismic reflection profiles.

onto the vertical component and cause significant effects on signal analysis [*Crawford and Webb*, 2000]. We extend the method developed by *Crawford and Webb* [2000] and use the horizontal records to predict and remove tilt noise from vertical component (S. Bell et al., Removing noise from the vertical component records of ocean bottom seismometers: Results from year one of the Cascadia Initiative, submitted to *Bulletin of the Seismological Society of America*, 2014) before calculating the pressure-to-displacement transfer functions.

In Figure 2, pressure records and tilting-corrected vertical displacement at station J44A are shown at the top. From the spectra of displacement and pressure, seafloor admittances from microseisms and earthquake-generated Rayleigh waves are calculated and shown at the bottom. From numerous records of microseisms, a robust transfer function can be estimated. As shown in Figure 2d, transfer functions estimated from both microseism and earthquake sources are essentially identical in the frequency range of 0.1 to 0.2 Hz. The advantage of using microseism noise is that microseism data are abundant and thus able to provide more reliable measurements of the admittance than Rayleigh waves generated by earthquakes. In fact, at short periods, i.e., in the microseism band, the Rayleigh waves in the "earthquake-generated" analyses are actually coming primarily from the background microseism noise rather than the earthquakes themselves.

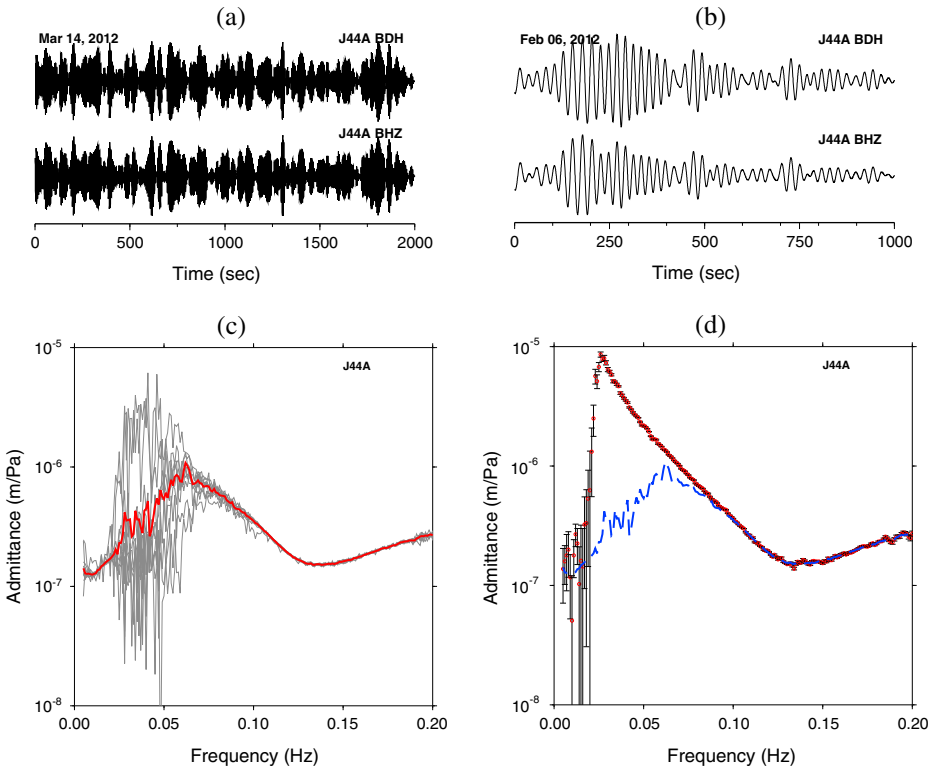

Figure 2. (a) Example of noise recorded at station J44A, band-pass filtered to 0.1–0.2 Hz. (b) Rayleigh waves of a teleseismic event occurred on 6 February 2012, band-pass filtered to 0.03–0.05 Hz. Top trace is pressure, and bottom is tilt-corrected vertical displacement. (c) Gray lines are admittance (amplitude of pressure-to-vertical transfer function) calculated using 12 days of noises; the admittance of each day is based on 9 to 30 2000 s long time series; red line is their mean. (d) Red dots are admittance calculated using nine records of Rayleigh waves generated by earthquakes; each record is 1000 s long; standard deviations at each frequency are plotted. Mean admittance from microseisms (blue dashed line) is plotted for comparison. Note that the admittance functions in Figures 2c and 2d are completely in agreement in the microseism band (0.1–0.2 Hz).

In Figure 3, we replot the admittance from the noise windows in a broader frequency band along with the phase of the transfer function (Figure 3b) and the coherence between pressure and the vertical component (Figure 3c). Note that at frequencies lower than 0.02 Hz, the band in which water infragravity waves are the dominant noise source, there is very little scatter of transfer functions from individual noise records and the coherence is high. There also is very little scatter at frequencies approximately from 0.1 to 0.2 Hz, where fundamental mode microseism Rayleigh waves dominate. In between these two high coherence bands, there is much scatter in what is generally termed the low-noise band. In this incoherent band, the admittance cannot be reliably estimated from noise samples. In both coherent bands, the phase shift is close to zero, as expected. Occasionally, we find a station with significant nonzero phase of the transfer function, indicating instrument response problems. We extend the Rayleigh wave admittance band using Rayleigh waves from a limited number of teleseismic earthquakes that fill in the low-noise band and extend to lower frequencies until infragravity waves begin to dominate the pressure records and the coherence with the vertical component Rayleigh waves drops (see Figures 2d and 3d). When the coherence drops, either in the earthquake windows when the infragravity waves begin to interfere or in the noise windows when the signals level fall entering the low-noise band, there are systematic biases in the admittance away from the pure fundamental mode Rayleigh wave transfer function. Therefore, we restrict our analyses to highly coherent (> 0.95) signals and combine the earthquake-generated Rayleigh wave transfer function ($f < 0.10$ Hz) with the microseism noise samples ($f > 0.10$ Hz) to broaden the frequency range.

The fall off in coherence at frequencies higher than 0.2 Hz (Figure 3d) is an indication of the presence of higher-mode Rayleigh waves. At these frequencies, individual higher modes can be identified in noise samples through ambient noise correlation analysis with amplitude comparable to the fundamental mode [e.g., *Harmon et al.*, 2007; *Takeo et al.*, 2014]. Whenever two or more modes are present with different transfer

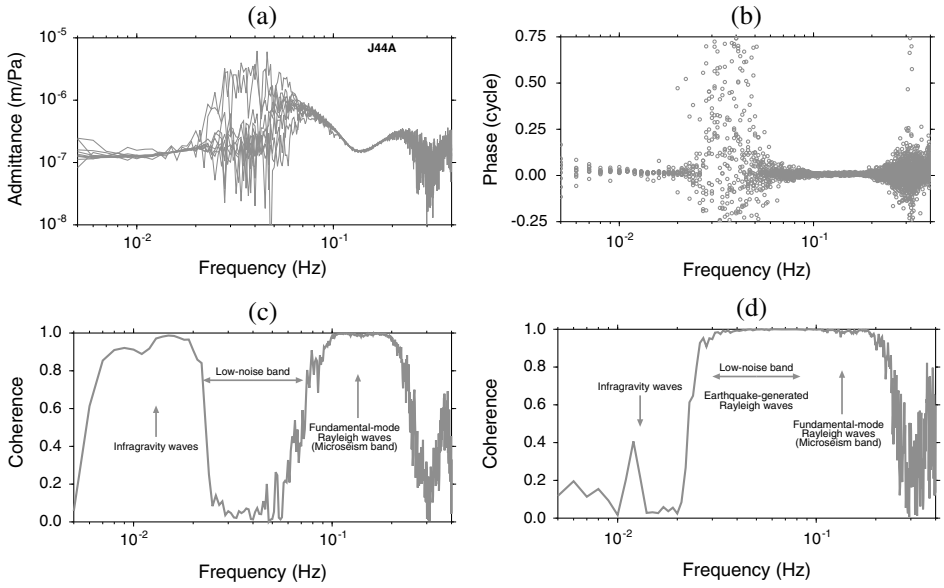

Figure 3. (a and b) The amplitude and phase of pressure-to-vertical transfer function at station J44A at frequencies from 0.005 to 0.4 Hz from the same time samples of noise used in Figure 2. (c) The coherence between pressure and vertical displacement calculated from noise samples. Pressure and displacement are highly coherent at frequencies less than 0.02 Hz where infragravity waves dominate the noise and at frequencies from 0.1 to 0.2 Hz where Rayleigh wave microseisms dominate the noise. In the low-noise band, pressure and displacement are incoherent. (d) The coherence calculated from earthquake-generated Rayleigh waves. Pressure and displacement are highly coherent in the low-noise band and the microseism band but are incoherent in the infragravity wave band due to the interference between Rayleigh waves and infragravity waves.

functions, interference between the modes will decrease the coherence and bias the transfer functions. As we will show later in section 5, the admittances are quite distinct for fundamental mode and the first higher mode. The secondary peak in coherence near 0.4 Hz is thought to be caused by near dominance of the first higher mode [*Sutton and Barstow*, 1990]. Mixing of fundamental-mode and higher-mode microseism waves will decrease the coherence and result in more scattered admittance functions at frequencies higher than 0.2 Hz (Figures 3a and 3d), so, in this study, we chose to investigate Rayleigh wave admittance from noise samples in the highly coherent band from 0.1 to 0.2 Hz to avoid contamination from higher-mode Rayleigh waves.

In Figure 4, we compare the transfer functions at three stations, J45A, J47A, and J54A, with similar water depth (2747 m, 2685 m, and 2667 m, respectively). Rayleigh wave D/P ratios observed at these three stations

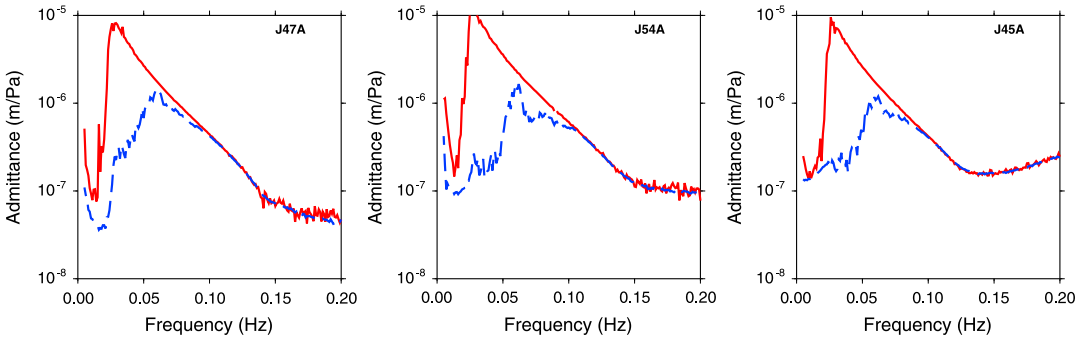

Figure 4. Observed seafloor compliance at station J47A, J54A, and J45A. Red lines are the admittance from earthquake-generated Rayleigh waves, and blue lines are the ones from noise. Water depth at all three station is similar, but sediment thickness beneath them is different (Figure 1), ranging from negligible at J47A to ~720 m at J45A. Rayleigh wave admittance functions at these stations are almost identical in the frequency range of 0.02–0.1 Hz but are very different in the microseism band (0.1–0.2 Hz) suggesting that Rayleigh wave admittance in the microseism band can be used to constrain marine sediment structure.

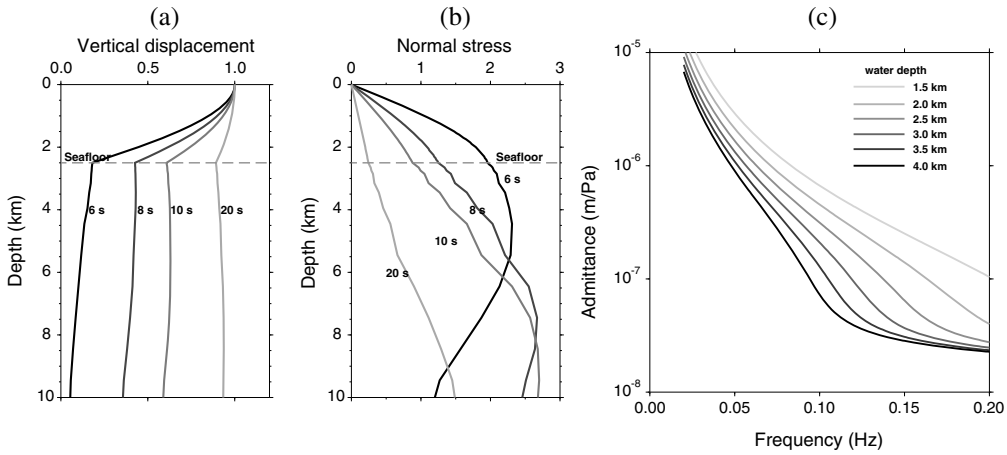

Figure 5. Examples of eigenfunctions—(a) vertical displacement, u_z, and (b) normal stress, τ_{zz}—for the fundamental-mode Rayleigh waves at periods of 6 s, 8 s, 10 s, and 20 s. The amplitude is normalized to the displacement at surface. Seafloor at 2.5 km depth is labeled by gray dashed lines. (c) Admittance at different water depth from 1.5 km to 4.0 km with constant crustal and mantle structure. Rayleigh wave admittance is dependent upon both wave period and water depth.

are almost identical in the period range of 0.02–0.1 Hz but are very different in the microseism band from 0.1 to 0.2 Hz (Figure 4). Since these three stations are known from previous seismic reflection profiles (Figure 1) to have distinctly different thicknesses of sediments beneath them, the observational results suggest that Rayleigh wave admittance in the microseism band can be used to constrain marine sediment structure.

3. Sensitivity of Rayleigh Wave D/P Ratio to Water Depth and Sediment Structure

In order to use Rayleigh wave admittance to invert for sediment structures, we investigated the sensitivity of the D/P ratio to water depth and sediments. Considering that the shear modulus in water is zero, the differential pressure above the seafloor, ΔP, is the wave-induced normal stress,

$$\Delta P(\omega) = \tau_{zz}(\omega) = K[u_{x,x}(\omega) + u_{z,z}(\omega)], \tag{3}$$

where τ_{zz} is the normal stress, K is the incompressibility of water, and $u_{i,j} = \partial u_i/\partial x_j$ are spatial derivatives of displacement. In the framework of surface waves, we can calculate the predicted Rayleigh wave admittance using a surface wave mode method. The amplitude of the transfer function—the ratio of vertical displacement to pressure—can be calculated directly from the eigenfunctions of Rayleigh waves, u_z and τ_{zz}, at the seafloor,

$$\eta(\omega) = \frac{u_z(\omega)}{\tau_{zz}(\omega)} = \frac{u_z(\omega)}{K[u_{x,x}(\omega) + u_{z,z}(\omega)]}. \tag{4}$$

We use the routines of *Herrmann* [1978] for flat Earth models to calculate the eigenfunctions. In an elastic and isotropic model, admittance of Rayleigh wave is a zero-phase complex function for the fundamental mode, but a π phase shift will be possible for higher modes due to the changing sign of eigenfunctions or their spatial derivatives at the seafloor. In the frequency range of 0.1–0.2 Hz, microseism noise is primarily fundamental-mode Rayleigh waves [e.g., *Sutton and Barstow*, 1990; *Harmon et al.*, 2007; *Yao et al.*, 2011], featured by very high coherence (> 0.95) between vertical displacement and pressure. At the appearance of higher modes, coherence will decrease due to the different admittance of fundamental mode and higher modes. So we only use Rayleigh wave admittance from microseism noise in the high coherence band and consider the fundamental modes in the theoretical calculations in this section.

In Figure 5, we show example eigenfunctions of fundamental-mode Rayleigh waves at periods of 6 s, 8 s, 10 s, and 20 s. From the eigenfunctions at the seafloor, we calculated theoretical admittance at frequencies from 0.02 to 0.2 Hz in models with water depth varying from 1.5 km to 4.0 km, keeping the crustal and mantle structure constant. For igneous crust and mantle in this study, we used a model (see Table 1) obtained from the East Pacific Rise [*Harmon et al.*, 2011], which is expected to have structure similar to the Juan de

Table 1. Model Parameters[a]

Model Layer	Thickness (km)	ρ (g/cm^3)	V_P (km/s)	V_S (km/s)
Water	local, fixed	1.030	1.500	0.0
Sediment	variable	2.000		
Upper crust	2	2.450	5.000	2.630
Lower crust	5	3.050	6.800	3.890
Uppermost mantle	20	4.326	7.913	3.270

[a]Crust and mantle structures are from study on the East Pacific Rise [*Harmon et al.*, 2011], *P* wave structure in sediment layer is from *Hamilton* [1979].

Fuca plate. The Rayleigh wave admittance is sensitive to water depth, and the amplitude increases with decreasing water depth and with increasing wave period. The increase with period is expected, because with increasing wavelength, the depth of penetration of Rayleigh waves increases and the spatial change in displacement (both horizontal and vertical) is more spread out, decreasing the normal stress and therefore increasing the ratio of displacement to pressure. In essence, at long periods, the whole water column moves uniformly up or down in concert with the seafloor so that there is little pressure variation. In the long period limit when the water column moves as a unit, the pressure to acceleration ratio approaches ρH, where ρ is the water density and H is the thickness of the water layer (S. Webb, personal communication, 2014). Similarly, as the seafloor shallows, the ratio of the water layer thickness to wavelength decreases, so the water layer moves more as a unit, again increasing the displacement at the seafloor while decreasing the gradient in displacement and therefore increasing the admittance. In deeper water, Rayleigh wave energy is more concentrated in the water column so that displacement decreases and the spatial gradient of displacement (normal stress) from water to crust increases and the admittance decreases.

We also calculated synthetic seafloor admittance in Earth models with different sediment settings to investigate the sensitivity to sediment properties. For our sediment models, *P* wave speed is calculated using the empirical depth-dependent relation estimated by *Hamilton* [1979] and density is chosen as a constant, 2.0 g/cm^3. The model parameters of igneous crust and mantle are shown in Table 1.

In Figure 6 are examples of Rayleigh wave eigenfunctions and synthetic admittance functions in models with a 2.5 km thick water layer and a 0.6 km thick sediment layer while average shear wave speed varies from 0.48 km/s to 0.68 km/s within the layer (assumed to be constant within the layer). Admittance functions are clearly sensitive to the shear wave speed of sediments, increasing with decreasing shear wave speed. Comparison between synthetic admittances calculated in models with and without sediment layers

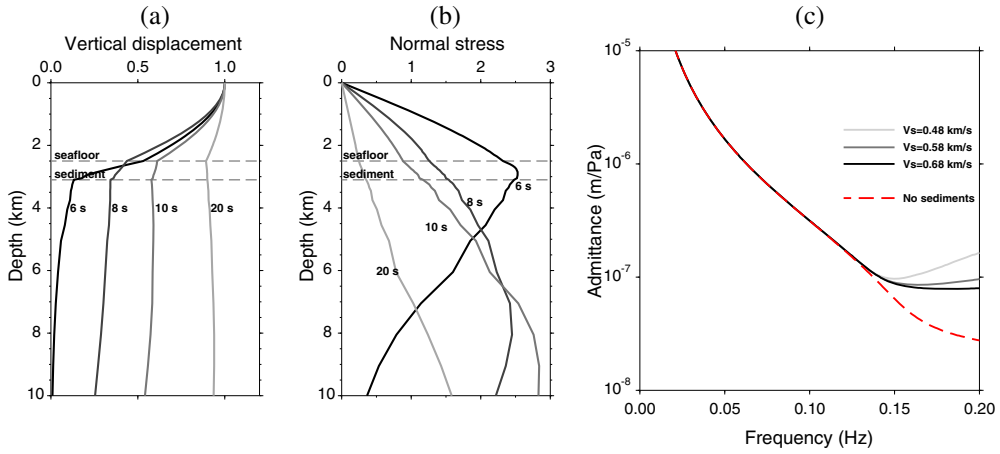

Figure 6. (a and b) Similar to Figure 5 but in a model with 0.6 km thick sediments. Water depth is held at 2.5 km. Seafloor and sediment basement interfaces are labeled by gray dashed lines. The soft sediment layer increases the admittance of Rayleigh waves in the microseism band. (c) Gray lines are admittance in models with different shear wave speed in sediments but constant sediment thickness, and the red dashed line is the reference admittance in a model without sediment. Rayleigh wave admittance is sensitive to the shear wave structure of marine sediments.

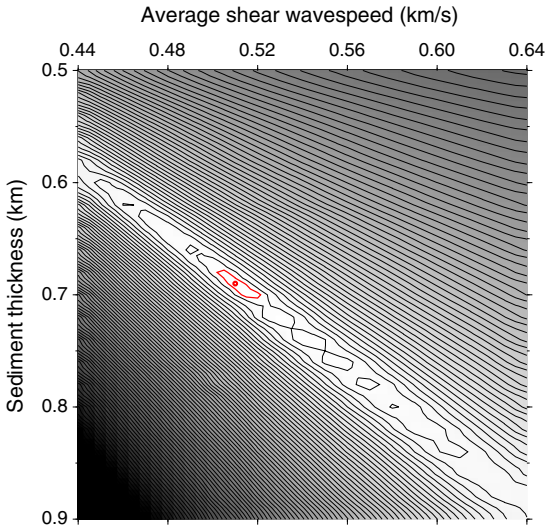

Figure 7. Grid search result of average shear wave speed and thickness of sediment beneath station J44A. These models assume constant shear wave speed within the sediment layer. Contour lines of the sum of the squares of the misfit to the admittance show a band of minimum values indicating a trade-off between shear wave speed and sediment thickness. Within this band, the total vertical shear wave traveltime through the sediment layer is nearly constant. In the vicinity of the absolute minimum (red dot), we perform a finer grid search to define the 95% confidence level (red contour).

shows large differences in the 0.1–0.2 Hz microseism band. Admittance functions at frequencies lower than 0.1 Hz show no sensitivity to sediments at this water depth and sediment thickness. If the sediments were much thicker, the effects would extend to longer periods. The presence of a sediment layer will tend to trap some of surface wave energy within it, increasing the displacement and the admittance of Rayleigh waves. The frequency range in which the transfer function is sensitive to sediments depends on the water depth, and thickness and wave speed of the sediment, and therefore varies from station to station. In conclusion, the Rayleigh wave admittance functions observed at deep water stations can be used to constrain shear wave speed and thickness of marine sediments.

4. Inversion of Rayleigh Wave Admittance

We selected 20 teleseismic events with moment magnitude between M_w 5.8 and 8.6 and removed the noise generated by tilting as much as possible from 24 h long vertical component records that contain the events. Due to varying noise levels at different stations, the number of events actually used to estimate admittance varied from 9 to 20. We manually picked the time windows for Rayleigh waves and microseism noise. For noise, the windows were selected to exclude any signals from local events or aftershocks or coda of teleseismic events. We combined the Rayleigh wave admittance from earthquakes at longer periods and the admittance from microseisms at shorter periods to form reliable Rayleigh wave admittance functions from 0.05 to 0.2 Hz. We then inverted the Rayleigh wave admittance function for sediment structure, initially assuming constant shear velocity within the sediment layer. To test the resolvability of admittance functions for shear wave speed and thickness, we did a grid search of these two parameters, with a third parameter, a constant scale factor that accounts for the imperfectly known amplitude responses of differential pressure gauges, adjusted at each point in the grid by least squares inversion. The constant scale factor is primarily constrained by the transfer function at frequencies below 0.10 Hz where there is little sensitivity to the sediments. Water depth was separately prescribed at each station based on the depth determined when precisely locating the OBSs by acoustic ranging.

For example, at station J44A, we calculated Rayleigh wave admittance functions (i.e., D/P ratio) for a set of models which are generated in thickness-wave speed space with 0.01 km/s spacing in shear wave speed and 0.02 km spacing in thickness. Forward models of predicted admittance were computed using Hermann's surface wave dispersion code [*Herrmann*, 1978]. Grid search results show a strip-like region of minimum misfit in parameter space, which implies strong trade-off between shear wave speed and thickness of sediments (Figure 7). Although the shear wave speed and thickness cannot be precisely constrained at the same time using the D/P ratio method, a best fitting thickness and wave speed can be identified. The red dot in Figure 7 is the inversion result, and the red ellipse is the 95% confidence interval, based on a finer grid search in the vicinity of the minimum.

For deep water stations in the first year data from the Cascadia Initiative, we performed a least squares inversion for shear wave speed of sediment while still doing a grid search on thickness to account for any nonlinear effects (changing thickness or shear velocity can significantly alter the eigenfunctions, introducing nonlinearity). Although we only invert for the assumed constant shear wave speed of sediments beneath each individual OBS, using a group of stations we find a well-resolved dependence of shear wave

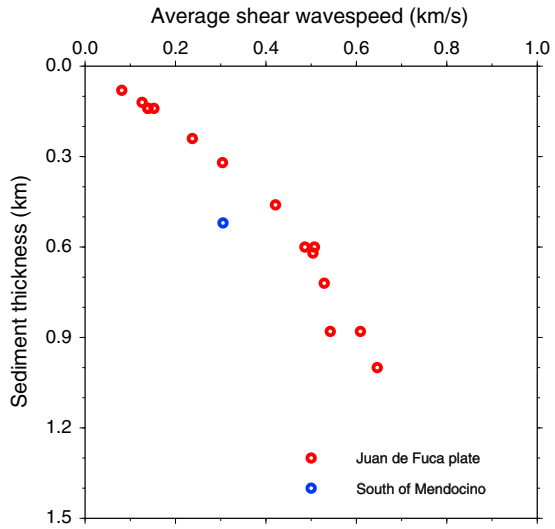

Figure 8. Summary of inversions for sediment thickness and velocity in constant shear velocity, single-layer models from Rayleigh wave admittance. The simple pattern of wave speed versus thickness of most of stations (red circles) indicates that velocity increases with depth of burial and suggests that there is probably a uniform profile of wave speed as a function of depth for sediments on the Juan de Fuca plate. Blue circle is "backbone" station G03A south of the Mendocino transform fault on the Pacific plate (Figure 1).

speed on the inferred thickness of the sediment layer on the Juan de Fuca plate (Figure 8). The average shear wave speed increases with increasing sediment thickness following a simple curve, clearly indicating, as expected, that shear wave speed increases with depth of burial, violating our initial simple assumption of constant shear wave speed within the sediment layer. This simple pattern suggests that there may be a common shear wave speed versus depth function for all the stations on the Juan de Fuca plate, with only sediment thickness varying. The outlier station G03A (Figure 8) located south of the Mendocino transform fault probably indicates a different source of sediment from the younger Juan de Fuca plate.

In the inversion of Rayleigh wave admittance, the control on sediment properties mainly comes from displacement at the seafloor. When there are sediments present, the increase in admittance at frequencies greater than 0.15 Hz is caused by increase in the displacement at the seafloor (compare the 6 s and 8 s curves in Figures 6a and 5a). A nonlinear relation between Rayleigh wave admittance and sediment structure is primarily caused by the sediments altering the eigenfunctions of vertical displacement as the sediments begin to act as a waveguide with increasing thickness or decreasing velocity. Due to the nonlinearity and sensitivity to very shallow structure, when the sediment wave speed increases with burial depth, it substantially alters the vertical displacement profile compared to a constant wave speed sediment layer with the same thickness and average velocity, yielding a different trade-off between sediment thickness and wave speed from that illustrated in Figure 7.

To obtain a more realistic sediment structure and to reduce the nonuniqueness in the single-station inversions, we simultaneously invert for a 1-D sediment wave speed profile for the whole Juan de Fuca plate and sediment thickness for each station. We assume that sediment on the Juan de Fuca plate has a depth dependence using a nonlinear function of the form

$$v_S(h) = (ah^2 + bh + cv_0)/(h + c), \tag{5}$$

where h is the depth below the seafloor. This empirical function is chosen to describe the dramatic increase of shear wave speed within the top 150 m in sediment and a relatively slow increase toward the bottom as sediment becomes thicker as shown in *Hamilton* [1979]. The starting wave speed parameters are listed in Table 2, and the wave speed of sediment at the seafloor, v_0, is chosen as 0.1 km/s [e.g., *Hamilton*, 1979; *Nolet and Dorman*, 1996]. Considering the trade-off between sediment thickness and wave speed, we first invert for the starting estimate of sediment thickness at each station, keeping the starting wave speed model fixed. Then we simultaneously invert for the sediment thickness at each station and the 1-D wave speed structure for whole region as described by the three constant parameters, a, b, and c. In addition, we include in the inversion a constant scale factor for each station to account for the uncertainty in amplitude calibration of each DPG. For a typical nonlinear inverse problem, we use a standard, linearized approach to find the solution [*Tarantola and Valette*, 1982],

$$\Delta\mathbf{m} = (\mathbf{G}^T\mathbf{C}_{nn}^{-1}\mathbf{G} + \mathbf{C}_{mm}^{-1})^{-1}(\mathbf{G}^T\mathbf{C}_{nn}^{-1}\Delta\mathbf{d} - \mathbf{C}_{mm}^{-1}[\mathbf{m} - \mathbf{m}_0]), \tag{6}$$

Table 2. Parameters for Shear Wave Speed[a] and Errors

	a (Error)	b (Error)	c (Error)
Starting model	0.54	0.37	0.29
Inversion model	0.02 (0.09)	1.27 (0.11)	0.48 (0.06)

[a] $v_S = (ah^2 + bh + cv_0)/(h + c)$, v_S is in km/s, and h is in kilometers.

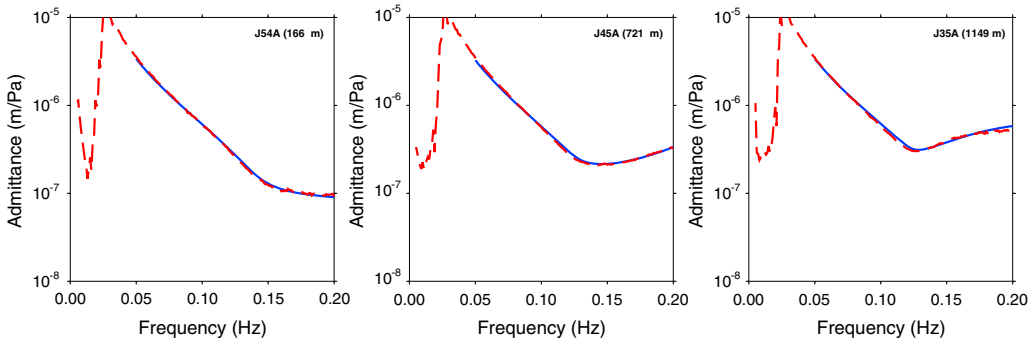

Figure 9. Comparison between observed Rayleigh wave compliance functions (red dashed line) and best fit synthetics (blue line) at three example stations, J54A, J45A, and J35A. Thickness of sediments underneath each station is listed in parentheses.

where $\mathbf{m}_0$ is the original starting model, $\Delta\mathbf{m}$ is the change relative to the current model $\mathbf{m}$, $\Delta\mathbf{d}$ is the difference between observed compliance and the predicted compliance from current model, $\mathbf{G}$ is the sensitivity matrix, i.e., partial derivatives relating changes of $\mathbf{d}$ to perturbations in $\mathbf{m}$, and $\mathbf{C}_{nn}$ and $\mathbf{C}_{mm}$ are the a priori covariance matrix of data and model, respectively. $\mathbf{C}_{mm}$ acts to damp or regularize the solution. In the inversion, we employed *a prior* 10% standard deviation of sediment thickness, 100% standard deviation for wave speed parameters, and 1000 for all constant scale factors. By choosing light damping on wave speed

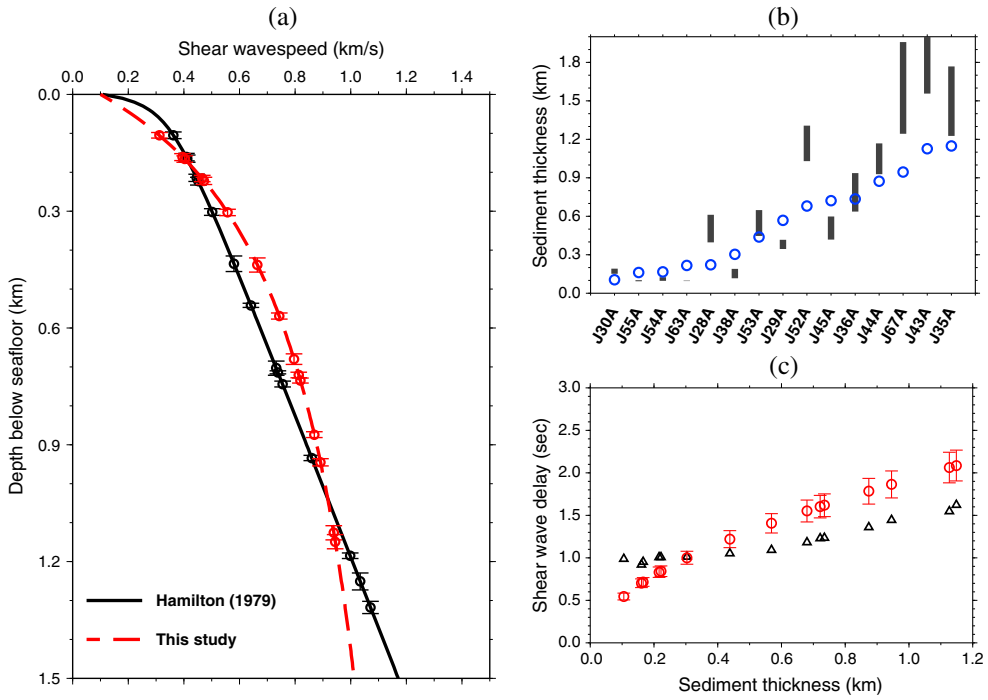

Figure 10. (a) Inversion results of 1-D shear wave speed structure (red dashed line) of sediments on the Juan de Fuca plate and associated thickness of sediments beneath each station (red circles). Error bars of thickness at each station are shown (the *x* axis positions of the thickness dots are arbitrarily assigned to fit on the profile as an indication of the depth control on velocity but are not an indication of the average velocity to that depth). The starting model based on data from *Hamilton* [1979] and the associated starting values of sediment thickness are shown for reference (black solid line and circles). (b) Sediment thickness at each station (blue circles). Minimum and maximum sediment thicknesses within 0.2° in radius from each station from NOAA's global map [*Divins*, 2003] are shown for comparison. (c) Vertical shear wave traveltime in sediments at each station (red circles) calculated from the inversion results of sediment wave speed and thickness. Estimated delays (black triangles) from one-layer constant sediment models (see Figure 8) do not agree with the variable velocity delays, indicating the importance of taking into account structure within the sediment column.

Table 3. Shear Wave Delay Times, Sediment Thickness, and Associated Errors at Individual Stations on the Juca de Fuca Plate[a]

Station	Delay (s)	Thickness (m)	Water Depth (m)
J30A	0.56 (0.04)	105 (6.1)	2839
J55A	0.70 (0.05)	161 (8.8)	2717
J54A	0.72 (0.05)	166 (8.4)	2667
J63A	0.83 (0.06)	216 (8.5)	2856
J28A	0.84 (0.06)	222 (9.1)	2865
J38A	1.00 (0.08)	303 (8.1)	2776
J53A	1.22 (0.10)	438 (18.2)	2688
J29A	1.41 (0.11)	569 (7.9)	2808
J52A	1.55 (0.13)	680 (13.6)	2620
J45A	1.60 (0.13)	721 (7.2)	2747
J36A	1.62 (0.13)	735 (7.1)	2838
J44A	1.79 (0.15)	874 (7.3)	2717
J67A	1.86 (0.16)	945 (9.5)	2556
J43A	2.06 (0.18)	1126 (18.4)	2650
J35A	2.09 (0.18)	1149 (18.3)	2661

[a]Water depth of each station also listed.

parameters and strong damping on thickness, we can stabilize the inversion without introducing unnecessarily large variations of sediment thickness caused by the trade-off between thickness and wave speed.

To account for the nonlinearity in inversion, we iterate until a stable result is reached. As with the single-station inversions, the data are the D/P ratios in the 0.05 to 0.2 Hz band. Station G03A is omitted in this regional inversion. Figure 9 shows there is a good fit between the predictions of the inverted model and observed admittance functions at three example stations with different sediment thicknesses of 166 m, 721 m, and 1149 m.

In Figure 10, we show the inversion model of shear wave speed of sediment on the Juan de Fuca plate. It shows a rapid increase with depth from 0.1 km/s at the surface of the seafloor to approximately 0.7 km/s at 500 m and then increases more slowly toward the bottom as sediments pile up thicker. For comparison, sediment thicknesses from the inversion (Figure 10b) are shown along with the range of sediment thicknesses within 0.2° in radius of each station from NOAA's global map (Figure 1) [*Divins*, 2003]. The wave speed parameters (Table 2), especially *a*, have relatively large uncertainties, partly because there is trade-off between these parameters. Although the parameters have large error bars, the resulting wave speed structure itself is very stable in the inversion. The large uncertainty in *a*, which controls the slope of the curve when *h* is large, means that the gradient deep in the sediment pile is poorly known; thus, this particular solution should not be used to extrapolate to areas with sediment thickness significantly greater than 1 km. The advantage of inverting a group of stations instead of single stations is that it can provide an estimate of the variation of wave speed with depth that allows a more accurate representation of the nonlinear effects of the sensitivity of the Rayleigh wave eigenfunctions to structure. The estimates of vertical shear wave traveltime through the depth-dependent sediment structure, i.e., the shear wave delay, are significantly different than the estimates for delay through the individual station inversions with constant shear wave speed (Figure 10c). Delays estimated from one-layer models are overestimated for thin layers and underestimated for thicker layers, resulting in smaller variations in delay times than for the more realistic models with gradients in shear velocity. The unrealistic one-layer, constant-velocity models result in strong biases in eigenfunctions at the seafloor, especially for normal stress, which is associated with the gradient of the displacement eigenfunctions.

From the result of shear wave speed model and sediment thickness, we can estimate shear wave delays caused by the sediment at all stations except those close to the Juan de Fuca ridge (with no or nonresolvable thin sediments). The error of delays can be calculated using a posteriori model covariance matrix (wave speed and thickness terms only) from the inversion,

$$\sigma^2 = \mathbf{Q}(\mathbf{G}^T\mathbf{C}_{nn}^{-1}\mathbf{G} + \mathbf{C}_{mm}^{-1})^{-1}\mathbf{Q}^T, \quad (7)$$

where **Q** is the sensitivity matrix made of partial derivatives of shear wave delay to model parameters, i.e., sediment thickness and wave speed parameters *a*, *b*, and *c*. In Table 3 and Figure 10c, we show the shear wave delays at 15 stations; most of the delays are larger than a half second due to the very low shear wave speed in the top hundred meters. At some stations, the delay can be as large as 2 s with approximately 1 km thick sediment. For any shear wave traveltime studies, there can be significant bias in the resulting tomography model if the sediment delays are not handled properly.

5. Discussion

The speed of sound in seawater is not a constant but a function of temperature, density, and salinity, and varies from 1.47 to 1.56 km/s [*Wong and Zhu*, 1995]. We calculated D/P ratios in models with a variety of

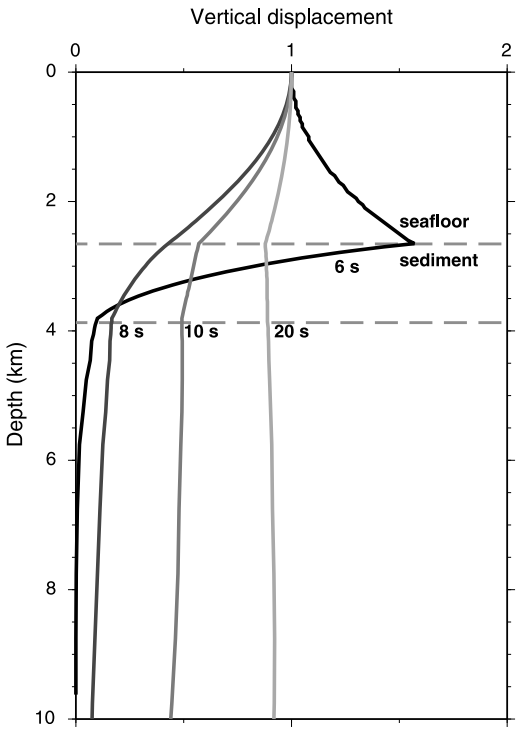

Figure 11. Example of eigenfunctions similar to Figure 6 but showing the presence of Scholte wave mode at short period (6 s) at station J35A. The Scholte interface wave is a different name for Rayleigh waves when the displacement concentrates on the boundary of liquid and solid. The transition frequency from Rayleigh wave to Scholte wave depends upon water depth and sediment thickness.

sound speed profiles without finding any noticeable effect in synthetic compliance at frequencies lower than 0.2 Hz; so for simplicity, we used a constant speed of 1.5 km/s for sound waves in the calculations. The structure of the igneous crust and upper mantle will affect our inversion results, but the fits to the shapes of the admittance curves in the 0.05 to 0.10 Hz frequency range is good, indicating that our assumed deeper velocity structure is adequate for the purposes of estimating sediment properties. The choice of shear wave speed at the seafloor, v_0, may have some effects on the inversion result. We found it necessary to either fix or very strongly damp this parameter in the inversion because of the nonlinear sensitivity to velocity right at the seafloor and the difficulty of accurately computing forward dispersion models and eigenfunctions with very thin, very slow sediment layers. The uncertainty of this constant parameter could be a large fraction of its assigned value, but considering the trade-off between wave speed parameters, the impact of this constant on the overall wave speed profile should be limited.

At the two stations with the thickest sediments, J35A and J43A, Scholte waves, a type of surface (interface) wave with displacement mostly concentrated on the liquid-solid boundary (Figure 11), begin to show up at frequencies higher than 0.167 Hz (6 s), i.e., within our analysis range. The frequency of the transition from Rayleigh wave to fundamental mode Scholte wave depends on water depth, sediment thickness, and wave speed structure (the fundamental mode Scholte wave is really the fundamental mode Rayleigh wave, just renamed to emphasize its different displacement function). The presence of Scholte waves in the microseism band does not affect the general behavior of compliance function (as shown in Figure 9, J35A) except for changing the curve of logarithm of admittance versus frequency from concave upward to concave downward in the 0.15 to 0.2 Hz band. Scholte waves can potentially provide even better constraints on the top part of sediments than Rayleigh waves due to their strong sensitivity to structure close to water-sediment interface.

As discussed in section 2, higher-mode Rayleigh waves may appear at frequencies around 0.2 Hz (5 s) and higher, and decrease the coherence between pressure and displacement (Figure 3). In Figure 12, we show the eigenfunctions and synthetic admittance of the first higher mode for station J35A, at water depth of 2661 m and sediment thickness of 1149 m. The admittances of fundamental and higher modes are significantly different at frequencies from 0.1 to 0.4 Hz when sediments are present, therefore the coherence between pressure and displacement decrease when the higher mode becomes important. The increase in coherence observed near 0.4 Hz (Figure 3) may be at least partially due to the increased similarity in transfer functions between the fundamental and first higher modes (Figure 12c) rather than being caused by the dominance of the first higher mode. Similarly, at the near ridge stations with thin sediments, the calculated transfer functions for the two modes are more similar to each other than when sediments are present and the drop in coherence at frequencies above 0.2 Hz is less pronounced.

Because the sediment layer can act as a waveguide, the behavior of higher modes is more complicated than for the fundamental mode. At certain frequencies when the pressure eigenfunctions are close to zero near the seafloor, the admittance function will have an infinite discontinuity. For simplicity, we chose 0.2 Hz as cutoff frequency at the higher end for all stations; however, for a few ridge and trench stations, the coherence decreases at frequency slightly lower than 0.2 Hz. In such cases, contamination of higher modes in

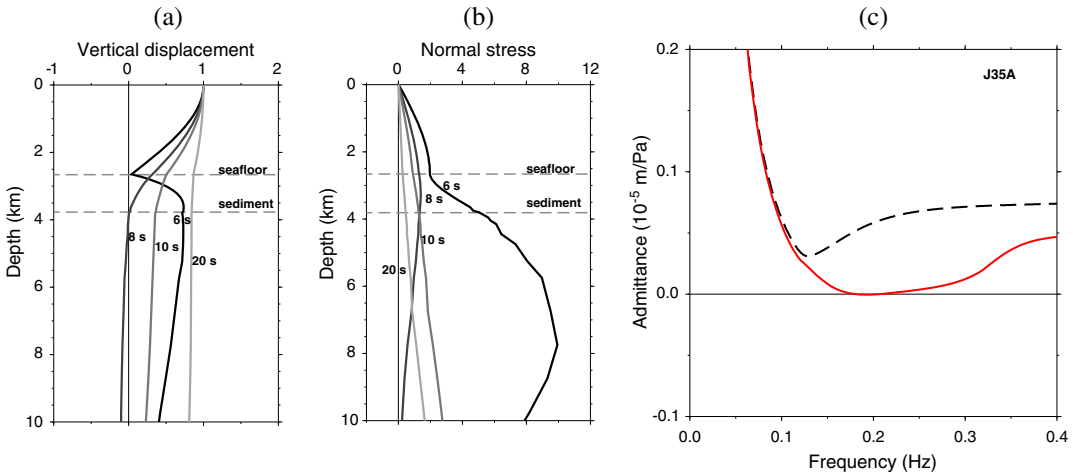

Figure 12. (a and b) Similar to Figure 6 but for first higher mode at station J35A. Water depth is 2661 m, and sediment thickness is 1149 m. Shear wave speed is from inversion and already shown in Figure 10. (c) The associated synthetic admittance function (red solid line). Admittance of fundamental mode Rayleigh waves is shown (black dashed line) for comparison. Admittance of different modes are distinct at microseism band and higher frequencies.

admittance measurements may be important. For a majority of stations we investigated, the coherence is higher than 0.95 throughout the microseism band between 0.1 to 0.2 Hz, therefore bias in our inversion results should be very limited. Ideally, the cutoff frequency can be selected according to the coherence at each station to exclude the higher-mode contaminations.

Comparison between our sediment thickness results with the smoothed regional map based on seismic reflection profiles (Figures 1 and 10b) shows that we are in a reasonably good agreement except where the thickness is rapidly changing near the trench. For instance, our estimates of thickness at J67A, J52A, and J43A are a few hundred meters thinner than predicted by the map. However, there are large local variations of depth to igneous basement caused by buried seamounts and ridges; the sediment thickness can vary dramatically over distances as little as 10 km [e.g., *Nedimović et al.*, 2008] and we do not have reflection profiles over each deployment location, so we do not know at this point whether there is any bias.

Stations close to the Juan de Fuca ridge are expected to have very thin sediments. In this paper, we find that sediments beneath stations J06A, J23A, J31A, J39A, J47A, and G30A are too thin to be resolvable using the Rayleigh wave compliance method. From a theoretical test, the limitation of sediment thickness to be detectable is about 60 m, so the stations listed above may have sediment thinner than the limit. Another reason we excluded these stations is that the crust and upper mantle structure close to the ridge are very different from structures away from the ridge.

Although the Rayleigh wave admittance and infragravity wave compliance methods are applied in very different frequency ranges using distinct waves, they can be used as good complementary methods to each other. For instance, at station J44A at water depth of 2717 m, the wavelength of well-observed infragravity wave varies from ~2950 m at 0.023 Hz to ~30 km at 0.005 Hz. For the highly coherent band combining both microseisms and earthquake sources (Figure 4), the wavelength of Rayleigh waves ranges from ~5 km at 0.2 Hz to 185 km at 0.02 Hz. In general, the Rayleigh wave admittance method can cover the depth penetration range of the infragravity waves-compliance method; although at longer periods and greater depths, the structure can be better inferred from the dispersion of the Rayleigh waves than from the admittance. The advantage of the admittance method using the microseism band is that it provides a local measurement beneath each station. Because infragravity waves and Rayleigh waves have different depth sensitivity to the subseafloor structure, the Rayleigh wave admittance method can be combined with the conventional compliance method to provide good constraints on marine sediments, as well as structure of the igneous crust and upper mantle. However, such joint applications are beyond the scope of this paper and will be discussed in separate ones.

In Figure 8, we notice an outlier station, G03A, in the sediment wave speed plot. This is a station located to the south of Mendocino transform fault on significantly older seafloor. Depending on the location,

sediments are formed from a mixture of biogenic and terrigenous sources and therefore may have different properties. The distinct result from G03A suggests that the source of sediment is very different from the source of sediment on the Juan de Fuca plate. With more data from the second year deployment of Cascadia Initiative, we should be able to reveal more details of the spatial pattern of sediment structure.

6. Conclusions

Our new Rayleigh wave admittance method presents a promising use of microseism noise on marine sediment imaging. From microseism noise, we can extract very reliable Rayleigh wave transfer functions at frequencies approximately from 0.1 to 0.2 Hz. Using the Rayleigh wave admittance from microseism noise and earthquake-generated Rayleigh waves, we inverted for a 1-D shear wave speed profile of sediment on the Juan de Fuca plate and associated sediment thicknesses beneath 15 deep water OBSs. Although the trade-off between sediment thickness and wave speed is significant, the shear wave delay time caused by sediment can be well constrained. From our results, most of the stations on the Juan de Fuca plate experience a delay larger than a half second, ranging up to about 2 s. This is a significant bias, and it is necessary to take it into account in traveltime tomography. For areas that have thicker marine sediments, for instance, near the coasts of the Gulf of Mexico and North Atlantic, this Rayleigh wave admittance method should be very useful for constraining the sediment structure.

Acknowledgments

The data used in this study are part of the Cascadia Initiative community experiment and are archived in the IRIS Data Management Center. We thank the Cascadia Initiative Expedition Team (CIET) and the Ocean Bottom Seismograph Instrument Pool (OBSIP) Institutional Instrument Centers for their efforts in collecting the data. The manuscript benefitted from constructive reviews by Wayne Crawford, Spahr Webb, an anonymous reviewer, and an Associate Editor. This research was supported by the National Science Foundation under grant OCE-1332876, and Y. Ruan was supported by a Brown University postdoctoral fellowship. The authors thank Robert Herrmann for providing the CPS package. Most figures are produced with GMT [*Wessel and Smith*, 1998].

References

Ardhuin, F., E. Stutzmann, M. Schimmel, and A. Mangeney (2011), Ocean wave sources of seismic noise, *J. Geophys. Res.*, *116*, C09004, doi:10.1029/2011JC006952.

Berge, P. A., S. Mallick, G. J. Fryer, N. Barstow, J. A. Carter, G. H. Sutton, and J. I. Ewing (1990), In situ measurement of transverse isotropy in shallow-water marine sediments, *Geophys. J. Int.*, *104*(2), 241–254, doi:10.1111/j.1365-246X.1991.tb02509.x.

Bradner, H. (1963), Probing sea-bottom sediments with microseismic noise, *J. Geophys. Res.*, *68*, 1788–1791.

Bromirski, P. D., R. A. Stephen, and P. Gerstoft (2013), Are deep-ocean-generated surface-wave microseisms observed on land?, *J. Geophys. Res. Solid Earth*, *118*, 3610–3629, doi:10.1002/jgrb.50268.

Cooper, R. I. B., and M. S. Longuet-Higgins (1955), An experimental study of the pressure variations in standing water waves, *Proc. R. Soc. London A*, *206*, 424–435.

Crawford, W. C. (2004), The sensitivity of seafloor compliance measurements to sub-basalt sediments, *Geophys. J. Int.*, *157*, 1130–1145, doi:10.1111/j.1365-246X.2004.02264.x.

Crawford, W. C., and S. C. Webb (2000), Identifying and removing tilt noise from low-frequency (< 0.1 Hz) seafloor vertical seismic data, *Bull. Seismol. Soc. Am.*, *90*, 952–963, doi:10.1785/0120070050.

Crawford, W. C., S. C. Webb, and J. A. Hildebrand (1991), Seafloor compliance observed by long-period pressure and displacement measurement, *J. Geophys. Res.*, *96*(B10), 16,151-16,160.

Divins, D. L. (2003), *Total Sediment Thickness of the World's Oceans & Marginal Seas*, NOAA National Geophysical Data Center, Boulder, Colo.

Ewing, J., J. A. Carter, G. H. Sutton, and N. Barstow (1992), Shallow water sediment properties derived from high-frequency shear and interface waves, *J. Geophys. Res.*, *97*(B4), 4739–4762, doi:10.1029/92JB00180.

Forsyth, D. W. (1985), Subsurface loading and estimates of the flexural rigidity of continental lithosphere, *J. Geophys. Res.*, *90*, 12,623–12,632.

Hamilton, E. L. (1971), Elastic properties of marine sediments, *J. Geophys. Res.*, *76*(2), 579–604.

Hamilton, E. L. (1979), V_P/V_S and Poisson's ratios in marine sediments and rocks, *J. Acoust. Soc. Am.*, *66*(4), 1093–1101.

Harmon, N., D. W. Forsyth, and S. C. Webb (2007), Using ambient seismic noise to determine short period phase velocities and shallow shear velocities in young oceanic lithosphere, *Bull. Seismol. Soc. Am.*, *97*, 2009–2023, doi:10.1785/0120070050.

Harmon, N., D. W. Forsyth, D. S. Weeraratne, Y. Yang, D. S. Scheirer, and S. C. Webb (2011), Mantle heterogeneity and off axis volcanism on young Pacific lithosphere, *Earth Planet. Sci. Lett.*, *311*, 306–315.

Herrmann, R. B. (1978), *Computer Programs in Earthquake Seismology, Volume 1: General Programs* (NTIS PB 292 462), edited by R. B. Herrmann, Department of Earth and Atmospheric Sciences, Saint Louis Univ., Saint Louis, Mo.

Kedar, S., M. S. Longuet-Higgins, F. W. N. Graham, R. Clayton, and C. Jones (2008), The origin of deep ocean microseisms in the north Atlantic Ocean, *Proc. R. Soc. London A*, *464*, 777–793, doi:10.1098/rspa.2007.0277.

Kugler, S., T. Bohlen, T. Forbriger, S. Bussat, and G. Klein (2007), Scholte-wave tomography for shallow-water marine sediments, *Geophys. J. Int.*, *168*, 551–570, doi:10.1111/j.1365-246X.2006.03233.x.

Longuet-Higgins, M. S. (1950), A theory of the origin of microseisms, *Philos. Trans. R. Soc. London A*, *243*, 1–35.

McKenzie, D., and C. Bowin (1976), The relationship between bathymetry and gravity in the Atlantic Ocean, *J. Geophys. Res.*, *81*, 1903–1915.

Munk, W. H., and D. E. Cartwright (1966), Tidal spectroscopy and prediction, *Philos. Trans. R. Soc. London, Ser. A*, *259*, 533–581.

Nedimović, M. R., S. M. Carbotte, J. B. Diebold, A. J. Harding, J. P. Canales, and G. M. Kent (2008), Upper crustal evolution across the Juan de Fuca ridge flanks, *Geochem. Geophys. Geosyst.*, *9*, Q09006, doi:10.1029/2008GC002085.

Nolet, G., and L. M. Dorman (1996), Waveform analysis of Scholte modes in ocean sediment layers, *Geophys. J. Int.*, *125*, 385–396.

Sutton, G. H., and N. Barstow (1990), Ocean-bottom ultra low-frequency (ULF) seismo-acoustic ambient noise: 0.002 to 0.4 Hz, *J. Soc. Am.*, *87*, 2005–2012.

Takeo, A., D. W. Forsyth, D. S. Weeraratne, and K. Nishida (2014), Estimation of azimuthal anisotropy in the NW Pacific from seismic ambient noise in seafloor records, *Geophys. J. Int.*, in press.

Tarantola, A., and B. Valette (1982), Generalized non-linear problems solved using the least-squares criterion, *Rev. Geophys. Space Phys.*, *20*, 219–232.

Tinivella, U., and F. Accaino (2000), Compressional velocity and Poisson's ratio in marine sediments with gas hydrate and free gas by inversion of reflected and refracted seismic data (South Shetland Island, Antarctica), *Mar. Geol.*, *164*, 13–27.

Webb, S. C., and W. C. Crawford (2010), Shallow-water broadband OBS seismology, *Bull. Seismol. Soc. Am.*, *100*(4), 1770–1778.

Wessel, P., and W. H. F. Smith (1998), New, improved version of the Generic Mapping Tools released, *Eos Trans. AGU*, *79*(47), 579–579, doi:10.1029/98EO00426.

Wong, G. S. K., and S. Zhu (1995), Speed of sound in seawater as a function of salinity, temperature and pressure, *J. Acoust. Soc. Am.*, *97*(3), 1732–1736.

Yamamoto, T., and T. Torii (1986), Seabed shear modulus profile invasions using surface gravity (water) wave-induced bottom waves, *Geophys. J. R. Astron. Soc.*, *85*, 413–431.

Yamamoto, T., M. V. Trevorrow, M. Badiey, and A. Turgut (1989), Determination of the seabed porosity and shear modulus profiles using a gravity wave inversion, *Geophys. J. Int.*, *98*, 173–182, doi:10.1111/j.1365-246X.1989.tb05522.x.

Yao, H., P. Gouedard, J. A. Collins, J. J. McGuire, and R. D. van der Hilst (2011), Structure of young East Pacific Rise lithosphere from ambient noise correlation analysis of fundamental- and higher-mode Scholte-Rayleigh waves, *C. R. Geosci.*, *343*(8-9), 571–583, doi:10.1016/j.crte.2011.04.004.